Journal of Membrane Science 588 (2019) 117193

Contents lists available at ScienceDirect

Journal of Membrane Science

journal homepage: www.elsevier.com/locate/memsci

Incorporation of an ionic liquid into a midblock-sulfonated multiblock polymer for CO_2 capture

Zhongde Dai[a], Luca Ansaloni[b], Justin J. Ryan[c,1], Richard J. Spontak[c,d], Liyuan Deng[a,*]

[a] Department of Chemical Engineering, Norwegian University of Science and Technology, Trondheim 7491, Norway
[b] Department of Sustainable Energy Technology, SINTEF Industry, Oslo 0373, Norway
[c] Department of Materials Science & Engineering, North Carolina State University, Raleigh, NC, 27695, USA
[d] Department of Chemical & Biomolecular Engineering, North Carolina State University. Raleigh, NC, 27695, USA

ARTICLE INFO

Keywords:
Sulfonated block polymer
Ionic liquids
Hybrid membranes
CO_2 separation

ABSTRACT

In the present work, hybrid block ionomer/ionic liquid (IL) membranes containing up to 40 wt% IL are prepared by incorporating 1-butyl-3-methylimidazolium tetrafluoroborate ([Bmim][BF_4]) into a midblock-sulfonated pentablock polymer (Nexar) that behaves as a thermoplastic elastomer. Various analytical techniques, including thermogravimetric analysis (TGA), Fourier-transform infrared (FTIR) spectroscopy, small-angle X-ray scattering (SAXS), and water sorption have been employed to characterize the resultant membrane materials. Single- and mixed-gas permeation tests have been performed at different relative humidity conditions to evaluate membrane gas-separation performance and interrogate the molecular transport of CO_2 through these membranes. Addition of IL to Nexar systematically enhances CO_2 permeability through membranes in the dry state. Introduction of water vapor into the gas feed further promotes CO_2 transport, yielding a maximum permeability of 194 Barrers and a maximum CO_2/N_2 selectivity of 128 under different test conditions. These results confirm that humidified Nexar/IL hybrid membranes constitute promising candidates for the selective removal, and subsequent capture, of CO_2 from mixed gas streams to reduce the environmental contamination largely responsible for global climate change.

1. Introduction

The primary culprit responsible for global climate changes is attributed to uncontrolled CO_2 [1], and numerous studies have specifically explored viable means by which to capture and subsequently utilize CO_2 [2]. Among the different methods presently used for CO_2 capture or separation, dense polymer membranes constitute a promising alternative to traditional CO_2 separation technologies (e.g., amine-based absorption and solid adsorption) due to their versatile modularity, small footprint, low or no chemical emissions, and ease of operation [3]. Prior studies of CO_2-selective polymer membranes have principally focused on developing new materials and processes to improve membrane separation efficiency [3]. Facilitated transport membranes [4,5], carbon membranes [6], mixed-matrix membranes [7], and hybrid membranes containing an ionic liquid (IL) [8] represent recent examples of several high-performance membranes. In previous efforts, a wide range of IL-based hybrid membranes has been reported wherein different ILs are physically incorporated into a variety of polymers, such as Pebax®, polyimide, poly(vinylidene fluoride-*co*-hexafluoropropylene), and poly(vinylidene fluoride) [8]. Upon judicious combination of polymer matrix and IL additive, significantly improved CO_2 permeability and selectivity can be simultaneously achieved. In these hybrid membranes, the IL is believed to act as a plasticizer that swells the host polymer, thereby resulting in higher CO_2 diffusivity and, consequently, higher CO_2 permeability. The accompanying high CO_2 selectivity derives from the chemical affinity between CO_2 and the IL, especially if the IL contains CO_2-philic functional groups [9].

In comparison to neutral polymers, ionomers or polyelectrolytes are expected to be more beneficial as polymeric matrices for IL-based hybrid membranes, since the intermolecular interactions between charged moieties on the polymer chains and IL molecules are significantly stronger than those involving uncharged polymers [10]. For instance, poly(IL)s have been studied extensively as host matrices for IL-based hybrid membranes for CO_2 separation [11]. Recently, analogous hybrid membranes employing Nafion, a highly fluorinated polyelectrolyte, have been investigated for CO_2 separation [12], and

* Corresponding author.
E-mail address: liyuan.deng@ntnu.no (L. Deng).
[1] Present address: Chemistry Division, United States Naval Research Laboratory, Washington, D.C., 20375, USA.

https://doi.org/10.1016/j.memsci.2019.117193
Received 13 May 2019; Received in revised form 14 June 2019; Accepted 15 June 2019
Available online 22 June 2019

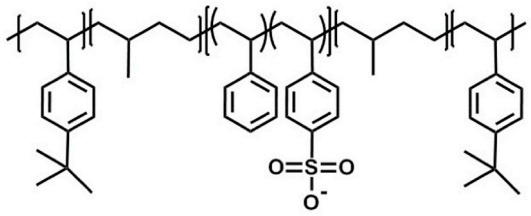

Fig. 1. Chemical structure of the midblock-sulfonated Nexar pentablock copolymer.

incorporation of an IL into Nafion greatly improves CO_2 permeability. Moreover, addition of IL is observed to induce a composition-dependent rearrangement of the Nafion nanostructure rather than simply swelling the polymer matrix. The IL-induced nanostructural transformation in charged polymer systems might create new diffusive pathways in hybrid membranes, and the new morphology provides access to enhanced molecular transport that favors CO_2 separation [12]. Another example of a charged polymer capable of forming a nanostructure composed of hydrophilic channels is Nexar (poly[*tert*-butylstyrene-*b*-(ethylene-*alt*-propylene)-*b*-(styrene-*co*-styrenesulfonate)-*b*-(ethylene-*alt*-propylene)-*b*-*tert*-butylstyrene]), a family of sulfonated pentablock polymers. Compared with Nafion, only the sulfonated polystyrene midblock of Nexar endows the material with hydrophilicity, while the outer hydrophobic blocks provide the strength of glassy poly(*tert*-butylstyrene) and the flexibility of hydrogenated polyisoprene (ethylene-propylene rubber, EPR). The chemical structure of Nexar is depicted in Fig. 1 and illustrates that the multifunctional macromolecule consists of 5 discrete chemical sequences, or blocks. While other styrenic diblock and triblock ionomers are also capable of self-organizing into ordered morphologies [13,14], Nexar is unique in that it is also a network-forming thermoplastic elastomer wherein the nonpolar glassy end-blocks responsible for physical cross-linking are uncompromised by the presence of a polar solvent, such as water. As a result, this material exhibits good dry/wet mechanical properties, as well as relatively high proton conductivity, water permeability and variable water uptake that depends on the degree of sulfonation (DOS) [15].

The molecular architecture of Nexar affords the possibility of varying chemical composition to generate different property-governing nanoscale morphologies [16]. Neutral block polymers spontaneously self-assemble into (a)periodic nanostructures due to thermodynamic incompatibility between the blocks [17]. Molecular factors affecting interfacial chain packing (*e.g.*, relative block size and monomer stiffness) regulate interfacial curvature and the equilibrium morphology. These same controls can be implemented with regard to the design of Nexar. In the specific case of block ionomers, the morphologies of Nexar can be solvent-templated due to the substantial chemical dissimilarity between the nonpolar and polar blocks [18–20]. For this reason, Nexar membranes can possess different nanostructures by tuning solvent selectivity. Nexar is predicted [21] to exhibit an alternating lamellar morphology at equilibrium on the basis of its composition. Use of a low-polarity mixed solvent for casting purposes, however, results in the formation of discrete, spherical ion-rich microdomains, whereas a more highly polar casting solvent yields a mixed morphology with continuous ion-rich pathways [19]. These morphologies can be further tuned through the use of solvent-vapor annealing [21]. Because of its amphiphilic nature, Nexar has been extensively investigated for various water-purification processes. Geise et al. [22] have systematically studied salt and water permeability, water uptake and salt diffusion in Nexar membranes for water desalination. It has also been employed to remove ionic pollutants from contaminated water in nanofiltration (NF). The most effective NF membrane reported [23] thus far can almost completely (> 99%) reject various divalent cations and also exhibits > 85% NO_3^- rejection and > 87% Na^+ rejection. Lastly, Nexar can be used for pervaporation dehydration of C2–C4 alcohols [24,25] and, compared to other polymeric membranes, affords a much higher total flux of isopropanol and *n*-butanol.

Although Nexar has shown tremendous promise for electrochemical and water-purification applications, it is rarely considered for gas separation. Fan et al. [26] have examined the transport of gases, liquids, and ions through Nexar, but their results suggest unimpressive performance with a CO_2 permeability lower than 30 Barrers and a CO_2/CH_4 selectivity lower than 7 in the dry state. Similar gas-permeation results are obtained when Nexar is complexed with metal ions (*e.g.*, Na^+, K^+ and Ca^{2+}). More recently, Ansaloni et al. [27] have discovered that both the morphology and the presence of water vapor can dramatically alter the gas-separation properties of Nexar, resulting in an ultrahigh NH_3 permeability exceeding 5000 Barrers, a high NH_3/N_2 selectivity of ≈1860, a moderate CO_2 permeability of ≈100 Barrers, and a CO_2/N_2 selectivity of ≈56. These encouraging results inspire us to improve the gas-transport properties of Nexar and broaden its utility in carbon capture, which is becoming increasingly critical with regard to global climate change. Herein, we explore the gas-transport properties of Nexar modified by the addition of an IL inherently possessing high CO_2 solubility and CO_2 selectivity over other gases, negligible vapor pressure and high thermal stability. Previous studies [19,21] have demonstrated that the morphology generated by the casting solvent used here yields continuous ionic pathways that serve as water channels, which are highly advantageous for uniform incorporation of the IL, as well as improved gas permeability. New IL-induced morphologies are therefore anticipated to consist of continuous hydrophilic channels, which would function as fast-transport pathways for CO_2. In this study, we explore the effect of incorporated IL on the nanoscale morphology, thermal stability and gas-separation properties (using single- and mixed-gas permeation tests) of hybrid Nexar/IL membranes. The overarching objective of this work is to elucidate relevant structure-property relationships of hybrid Nexar/IL membranes intended for CO_2 separation under different relative humid (RH) conditions.

2. Experimental

2.1. Materials and membrane preparation

A single grade of poly[*tert*-butylstyrene-*b*-(ethylene-*alt*-propylene)-*b*-(styrene-*co*-styrenesulfonate)-*b*-(ethylene-*alt*-propylene)-*b*-*tert*-butylstyrene] (Nexar) was kindly provided in film form by Kraton Polymers (Houston, TX, USA). The molecular characteristics of this block ionomer, provided by the manufacturer, were described earlier [20], and its ion exchange capacity (IEC) was reported as 2.0 meq/g. 1-Butyl-3-methylimidazolium tetrafluoroborate ([Bmim][BF_4], 97%) and anhydrous tetrahydrofuran (THF) were purchased from Sigma-Aldrich (Oslo, Norway) and used as-received. High-purity single gases, CH_4 (> 99.999%), CO_2 (> 99.999%) and N_2 (> 99.999%) gases, as well as CO_2/N_2 gas mixtures, were obtained from AGA (Oslo, Norway). The Nexar film was dissolved in THF to yield a 2–4 wt% solution. The [Bmim][BF_4] was added to the solution to achieve a desired mass percent relative to Nexar (ω_{IL}) and stirred for at least 2 h. It is worth mentioning that other ILs have also been investigated here as additives including 1-Ethyl-3-methylimidazolium acetate ([Emim][Ac]), 1-Butyl-3-methylimidazolium tricyanomethanide ([Bmim][TCM]), 1-Ethyl-3-methylimidazolium bis(trifluoromethylsulfonyl)imide ([Emim][Bf_2N], all obtained from IoLiTec (Heilbronn, Germany), and a few amino acid-based ILs synthesized in our lab. Unfortunately, the [Bmim][BF_4] was found to be the only IL that could form homogeneous hybrid membranes with the Nexar polymer. Therefore, [Bmim][BF_4] was selected in the present study. Each Nexar/IL solution was poured into a Teflon Petri dish and subsequently covered with a glass Petri dish to reduce the rate of solvent evaporation. After about 2 weeks of solvent removal under quiescent ambient conditions, each resulting film, measuring 30–40 μm thick, was dried under vacuum at 30 °C for at least 6 h before any characterization tests were performed.

2.2. Membrane characterization

For thermogravimetric analysis (TGA), a thermo-microbalance from Netzsch (TG 209F1 Libra) was employed to ascertain the thermal stability of Nexar/IL films. Samples were heated from ambient temperature to 600 °C at a heating rate of 10 °C/min under N_2. Fourier-transform infrared (FTIR) spectroscopy of Nexar/IL films was conducted over the wavelength range of 650–4000 cm^{-1} in attenuated total reflectance (ATR) mode on a Thermo Nicolet Nexus spectrometer equipped with a diamond crystal. Each chemical spectrum reported here is background-corrected and represents the average of 32 scans. Morphological features of Nexar/IL films were analyzed by small-angle X-ray scattering (SAXS) performed on beam-line 12-ID-B in the Advanced Photon Source at Argonne National Laboratory. Details regarding the experimental setup and collection conditions were previously provided [12,27]. Two-dimensional scattering patterns were azimuthally integrated and collapsed to one-dimensional scattering profiles with intensity expressed in terms of the scattering vector, $q = (4\pi/\lambda)\sin\theta$, where θ denotes half the scattering angle. Water uptake into the Nexar/IL films was investigated under equilibrium and time-dependent conditions. Equilibrium uptake was ascertained by placing each membrane in a closed volume saturated with water vapor at ambient temperature and pressure. The sample weight was monitored until it remained constant, and the equilibrium water uptake (Ω_{H_2O}) was taken as the average of two such measurements (differing by less than 5%).

Time-dependent water uptake was examined by pressure decay, as depicted in Fig. 2. The mass of the membrane samples used for time-dependent water uptake test was normally 0.03–0.05 g. After each membrane was placed in Chamber 2, the entire system was evacuated and the valve separating the two chambers was closed. Once water vapor was subsequently introduced into Chamber 1 to a desired pressure, the interchamber valve was opened and the pressure in Chamber 2 was continuously monitored. The water uptake was determined from the pressure change between the two chambers until equilibrium was reached. Except for the initial evacuation step, this procedure was repeated several times in discrete steps by increasing the pressure of water vapor in Chamber 1 until a complete water sorption isotherm was generated. Water sorption at each step was calculated from

$$\omega_{H_2O,i} = \frac{\Delta m_{H_2O,i}}{m_{pol}} = \frac{[p_{i,start}\cdot V_1 + p_{i,\infty}\cdot V_2 - p_{i,\infty}\cdot(V_1 - V_2)]\cdot M_{H_2O}}{m_{pol}\cdot R\cdot T} \quad (1)$$

where $\omega_{H_2O,i}$ represents the water uptake at step i, $\Delta m_{H_2O,i}$ is the water mass absorbed in step i, $p_{i,start}$ is the starting pressure of Chamber 1 in step i, and $p_{i,\infty}$ is the equilibrium pressure of Chambers 1 and 2 in step i.

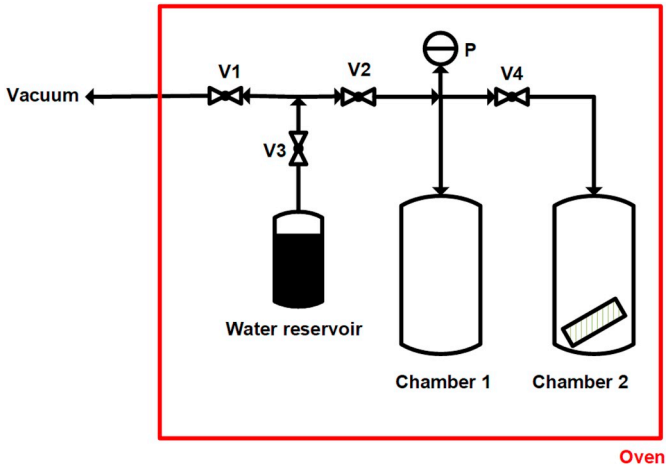

Fig. 2. Schematic diagram of the pressure-decay setup employed here to measure water sorption.

In addition, V_1 and V_2 denote the volumes of Chambers 1 and 2, respectively, and R, M_{H_2O} and T correspond to the universal gas constant, molar mass of water (18 g/mol) and absolute temperature, respectively. The diffusivity (D) of water could likewise be discerned under Fickian conditions from absorption kinetics according to

$$\frac{m_{sample}}{m_{sample,\infty}} = 1 - \sum_n \frac{8}{(2n+1)^2\cdot\pi^2}\cdot\exp\left[\frac{-D\cdot(2n+1)^2\cdot\pi^2\cdot t}{L^2}\right] \quad (2)$$

where m_{sample} and $m_{sample,\infty}$ denote the sample mass at a specific time (t) and at equilibrium, respectively, and L is the membrane thickness. Membrane thicknesses were measured with a Digitix II thickness gauge (NSK). At least 10 points were sampled for each membrane, and the average was used as L in relevant calculations. All water sorption tests were conducted at 35 °C and a RH level not exceeding 80% to avoid internal condensation.

A custom-built single-gas permeation system, schematically depicted in Fig. 3, was utilized to discern the permeabilities of CO_2 and N_2 at different RH levels controlled from 0 to 90%. For completeness, RH is defined as the ratio of the water-vapor pressure in the chamber to the saturated water-vapor pressure (p^*)at the same temperature. The temperature dependence of p^* (in mbar) is given by [28]:

$$p^* = 1.333\cdot\exp\left(20.386 - \frac{5132}{T}\right) \quad (3)$$

The entire system was maintained in a thermostatic chamber to ensure isothermal conditions. Upon insertion of a membrane into the membrane module, the system was evacuated overnight, and water vapor was subsequently introduced at a desired RH level to saturate the membrane. A few hours were typically needed for saturation to ensure a uniform water concentration profile in the membrane. The system was stabilized when the water-vapor pressure became identical on both sides of the membrane and kept unchanged. After this initial stabilization, a feed gas with the same RH as that of the membrane module was injected into the system to initiate a permeation test. Single-gas permeability (P_s) values, routinely expressed in Barrers (1 Barrer = 10^{-10} cm^3(STP) cm s^{-1} cm^{-2} [cm Hg]$^{-1}$), were extracted from the pressure change in the downstream side [29]. More specifically, P_s was calculated from the difference between upstream and downstream pressures (p_u and p_d, respectively) and the rate of downstream pressure increase (dp/dt) after reaching steady state, *viz.*,

$$P_s = \left[\left(\frac{dp_d}{dt}\right)_{t\to\infty} - \left(\frac{dp_d}{dt}\right)_{leak}\right]\cdot\frac{V_d}{A\cdot R\cdot T}\cdot\frac{L}{(p_u - p_d)} \quad (4)$$

Here, V_d is the downstream volume and A is the effective permeation area of the membrane (fixed at 19.5 cm^2). The leakage rate $\left(\frac{dp_d}{dt}\right)_{leak}$ of ambient air into the permeate-side reservoir was measured when all the valves were closed to isolate the evacuated membrane cell. The corresponding ideal permeability selectivity was determined from $\alpha^i_{AB} = \frac{P_A}{P_B}$, where P_A and P_B correspond to the permeabilities of gas species A and B, respectively. Each membrane was tested in duplicate with a relative error of less than 10% (reported values correspond to the average acquired at 35 °C with an upstream feed pressure of ≈1 bar).

Mixed-gas permeation was also analyzed on the basis of the conventional constant-pressure/variable-volume protocol [30]. In the present study, a 10/90 v/v CO_2/N_2 gas mixture was used as the feed gas, whereas pure CH_4 served as the sweep gas. Since helium served as the carrier gas for the gas chromatograph (GC) in this work to determine gas compositions, CH_4 was employed as the sweep gas instead of helium to reduce the error in composition analysis. The pressures on the feed and sweep sides of each membrane were maintained at 2.0 and 1.05 bar, respectively, for all tests performed. The mixed-gas permeability of the ith gas species was obtained from

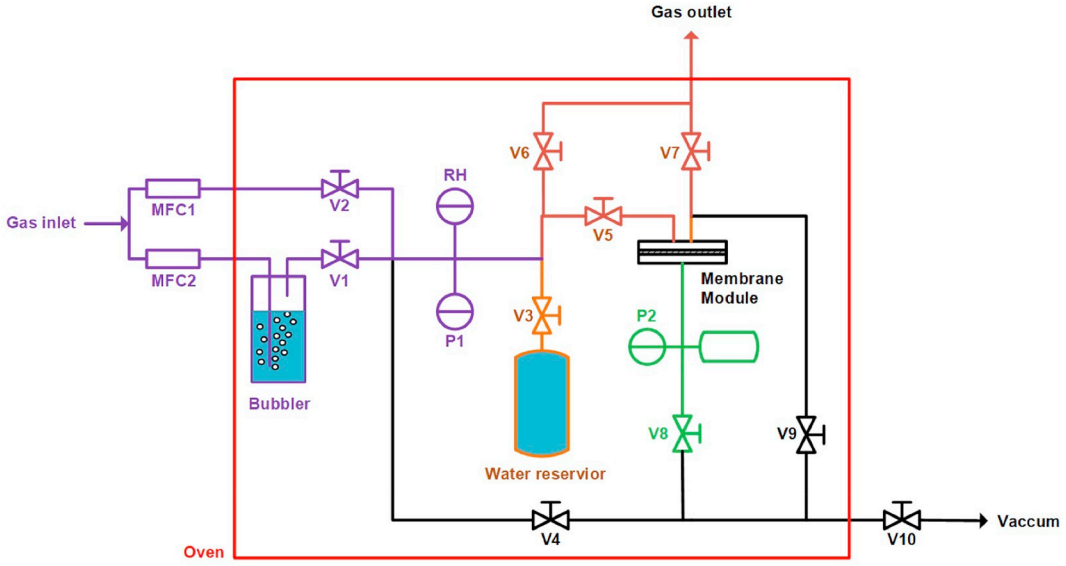

Fig. 3. Schematic depiction of the permeation apparatus used to measure single-gas permeation under controlled humidity conditions.

$$P_{m.i} = \frac{N_{perm}\cdot(1 - y_{H_2O})\cdot y_i \cdot L}{A\cdot(\langle p_{i,feed}, p_{i,ret}\rangle - p_{i,perm})} \quad (5)$$

where N_{perm} is the total permeate flow, y_{H2O} and y_i are the mole fraction of water and species i in the permeate, and $p_{i,feed}$, $p_{i,ret}$ and $p_{i,perm}$ identify the partial pressures of the ith species in the feed, retentate, and permeate, respectively. The corresponding mixed-gas separation factor was discerned from $\alpha_{i/j} = \frac{y_i / x_i}{y_j / x_j}$.

3. RESULTS and DISCUSSION

3.1. Thermal analysis

The thermal properties of neat Nexar and Nexar/IL hybrid membranes are presented for comparison in Fig. 4. For simplicity, the hybrid membranes are designated as Nexar/ILω_{IL}. An immediate distinction in this figure is that the IL is substantially more stable at temperatures below its decomposition temperature (T_d) and likewise possesses a higher T_d relative to neat Nexar and its blends with IL. Mass loss at

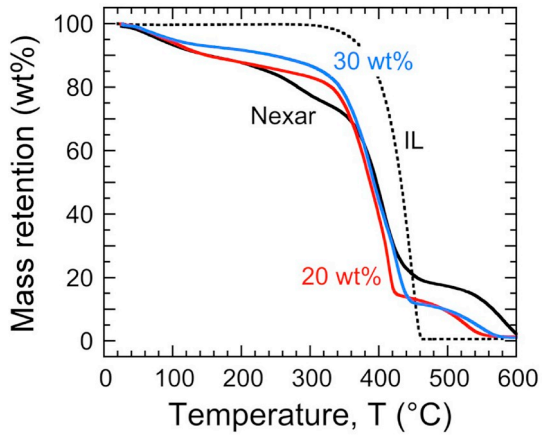

Fig. 4. Mass retention presented as a function of temperature, as measured by TGA, for neat Nexar and the [Bmim][BF_4] IL, as well as Nexar/IL hybrid materials (labeled according to ω_{IL} and color-coded). (For interpretation of the references to color in this figure legend, the reader is referred to the Web version of this article.)

$T < T_d$ in the case of Nexar and Nexar/IL membranes is most likely due to a combination of residual water outgassing at temperatures below ≈120 °C and thermal degradation of the sulfonic acid groups. The onset of decomposition lies in the vicinity of 320 °C. Regarding the first stage, ionomers commonly contain residual water [31]. Fan et al. [26] have found that pre-conditioning Nexar at 120 °C for 20 min can be used to remove residual water from the polymeric matrix. In the second stage, the extent and uniformity of mass loss is clearly composition-dependent, and the thermal stability increases with IL content in the hybrid membranes. A third stage occurs from about 300 to 450 °C, over which an abrupt and precipitous decrease in mass retention is observed presumably due to thermal degradation of the Nexar backbone, as well as the [Bmim][BF_4] IL (for which $T_d \approx 400$ °C, in favorable agreement with the reported [32] temperature of 403 °C). At $T > 450$ °C, the IL appears to completely decompose into gaseous products so that its mass retention approaches 0 wt%, whereas Nexar and its hybrid membranes undergo thermally-driven chemical changes into complex sulfur and carbonaceous compounds that are capable of persisting up to 550–600 °C before they, too, further decompose into gaseous products at higher temperatures.

3.2. Chemical analysis

The chemical signatures of Nexar and several Nexar/IL hybrid membranes have been examined by FTIR spectroscopy, and representative spectra acquired from 650 to 4000 cm^{-1} for Nexar and Nexar/IL hybrid membranes at four different IL concentrations are provided in Fig. 5. The neat Nexar membrane displays a broad peak in the vicinity of 3500 cm^{-1} due to hydroxyl stretching and vibrations from the sulfonated polystyrene groups. The three peaks between 2800 and 3000 cm^{-1} are associated with asymmetric and symmetric CH-stretching vibrations from the methyl groups, while the peaks near 1400–1500 cm^{-1} are attributed to C=C stretching from the phenyl rings. Peaks evident at 1006, 1035, 1126, and 1411 cm^{-1} constitute characteristic peaks of the SO_3^- moiety. The remaining peaks observed below 900 cm^{-1} are indicative of CH- out-of-plane deformation in the polystyrene repeat units. Upon addition of the [Bmim][BF_4] IL, a broad peak between *ca.* 3120 and 3200 cm^{-1} likely reflects quaternary amine salt formation with tetrafluoroborate. Peaks at 1655 and 1466 cm^{-1} are due to C=C and C=N stretching, and the pronounced peaks at about 1200 and 1100 cm^{-1} are attributed to in-plane bending vibration from methyl groups [33]. As expected, peak intensities change according to

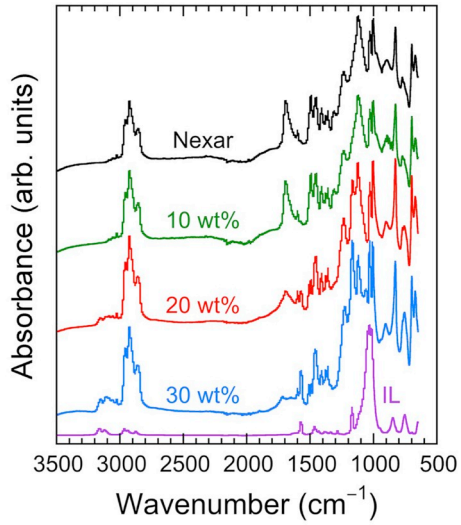

Fig. 5. FTIR spectra of neat Nexar, the [Bmim][BF_4] IL and Nexar/IL hybrid materials (labeled according to ω_{IL} and color-coded). (For interpretation of the references to color in this figure legend, the reader is referred to the Web version of this article.)

blend composition. The intensity of the peak at ≈1700 cm^{-1}, which reflects C–C stretching from the aromatic rings in Nexar [26], gradually decreases as the IL content increases. Since no new peaks appear in the Nexar/IL hybrid membranes, we infer that no chemical interactions exist between Nexar and [Bmim][BF_4].

3.3. Morphological analysis

A series of SAXS profiles collected from Nexar and Nexar/IL hybrid membranes cast from THF is presented in Fig. 6. As demonstrated elsewhere [19], the choice of casting solvent is critically important with regard to morphological development in Nexar since the hydrophilic and hydrophobic blocks are so chemically dissimilar. Use of a mixed solvent composed of, for example, toluene and isopropanol in which toluene is the major constituent yields micelles, each with a polar core and nonpolar corona, upon self-assembly in solution. Complementary

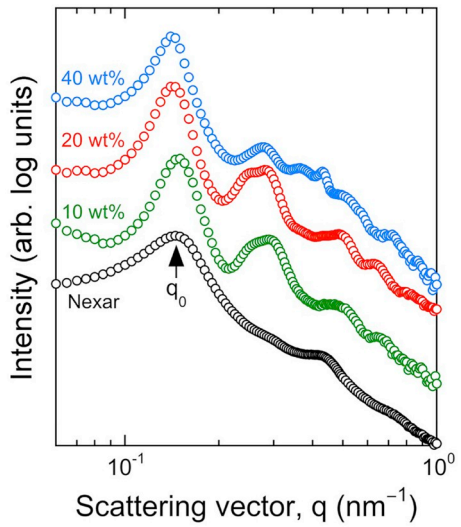

Fig. 6. SAXS intensity profiles presented as a function of scattering vector (q) acquired from THF-cast Nexar and Nexar/IL hybrid membranes (labeled according to ω_{IL} and color-coded). (For interpretation of the references to color in this figure legend, the reader is referred to the Web version of this article.)

SAXS and small-angle neutron scattering (SANS) analyses of these micelles reveal [20] that the micelles are swollen with isopropanol and the extent of swelling is dependent on the solution composition. This micellar morphology is largely retained in dried films, providing clear evidence for solvent templating. In the case of a single solvent such as THF, however, such partitioning does not occur, and the resultant cylindrical + lamellar morphology in dried films more closely resembles the equilibrium lamellar morphology predicted from dissipative particle dynamics (DPD) simulations [21]. Solvent-vapor annealing of Nexar possessing either a micellar or mixed morphology in THF at ambient temperature quickly promotes nanostructural refinement (over the course of minutes) into well-ordered and, in some cases, well-oriented lamellae [34]. The SAXS profile for Nexar included in Fig. 6 displays a poorly organized nanostructure with a broad principal peak located at q_o = 0.146 nm^{-1}, a weak second peak at 0.290 nm^{-1} and a broad third peak centered at 0.431 nm^{-1}. According to Bragg's law, the microdomain periodicity (d), given by $2\pi/q_o$, is 43.0 nm, which agrees favorably with previous reports [21] of Nexar cast from THF (d = 44.5 nm).

Since the [Bmim][BF_4] IL is highly hydrophilic, it is expected *a priori* to localize in the polar microdomains containing sulfonic acid groups. The first and obvious effect of IL incorporation into Nexar is that the nanostructural order, signified by the number of discernible scattering peaks, is significantly improved with at least four higher-order peaks observed beyond q_o (the broad peak with a shoulder located between 0.2 and 0.4 nm^{-1} in the films with 10 and 20 wt% IL is interpreted as two overlapping peaks due to two coexisting morphologies). We return to discuss the position of these peaks below. The next effect of added IL is that the principal peak positioned at q_o systematically shifts to lower q as the fraction of IL is increases. Values of d extracted from these peak positions range from 42.5 to 44.6 nm and confirm that the Nexar morphology swells upon addition of the [Bmim][BF_4] IL. Similarly, the shift to lower q in the third peak in the profiles corresponding to 10 and 20 wt% IL and the second peak in the profile from the specimen with 40 wt% IL is likewise indicative of nanostructural swelling. The peak positions relative to q_o in each scattering profile can be used to discern the morphology present. Normalized peak positions (expressed as q/q_o up to ≈3 to avoid confusion of the structure factor with the form factor) for the four scattering profiles are listed below for each value of ω_{IL}:

(0 wt%) 1.00, 1.99, 2.95
(10 wt%) 1.00, 1.74, 1.99
(20 wt%) 1.00, 1.73, 1.98
(40 wt%) 1.00, 1.74, 1.99, 2.62, 3.06

From these peak positions, we suspect that the neat Nexar specimen likely possesses a lamellar morphology, which has been previously observed [19,21] in this material by electron microscopy, although the lack of additional scattering peaks hinders unambiguous assignment. The morphologies in the Nexar/IL10 and Nexar/IL20 membranes appear to be a combination of cylinders and lamellae (which is due to the presence of the second peak [shoulder] but no higher-order peaks and which has also been reported [19] for neat Nexar), whereas the morphology in the hybrid membrane with 40 wt% IL appears to be completely cylindrical. We therefore conclude that addition of the [Bmim][BF_4] IL to Nexar promotes nanostructural swelling, which verifies that the IL is incorporated within the block ionomer matrix, as well as morphological reorganization by residing exclusively in, and swelling, the hydrophilic regions.

3.4. Water sorption

Water sorption tests have been performed at 35 °C with water activity (p/p^*) ranging from 0 to ≈0.8. In this interval, the response of Nafion/IL hybrid membranes differing in ω_{IL} appears to be complex in

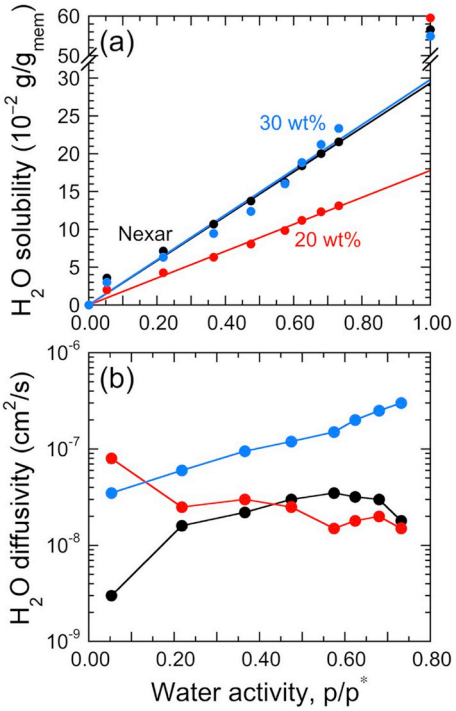

Fig. 7. Water (a) solubility and (b) diffusivity of neat Nexar and Nexar/IL hybrid membranes presented as functions of water activity (p/p^*) at 35 °C (labeled according to ω_{IL} and color-coded). The solid lines in (a) are linear regressions to the data, whereas those in (b) serve to connect the data. (For interpretation of the references to color in this figure legend, the reader is referred to the Web version of this article.)

Fig. 7a. Relative to the behavior of neat Nexar (which implies a nearly linear dependence), the membrane with 20 wt% [Bmim][BF_4] IL sorbs slightly less water, whereas the Nexar/IL30 membrane sorbs slightly more water. These relatively subtle differences most likely reflect changes in the membrane morphologies, which are observed, according to SAXS (see Fig. 6), to change upon IL incorporation. Extrapolation of the linear relationships evident in Figs. 7a to 100% RH yields the following values of Ω_{H_2O} (in %): 29.3 (ω_{IL} = 0%), 17.8 (ω_{IL} = 20%) and 29.8 (ω_{IL} = 30%). Measured values of Ω_{H_2O} included in Fig. 7a are higher than these extrapolations, clustered around 60%. Compared to Relative to previous studies of water sorption in this particular grade of neat Nexar [22,35] that indicate the equilibrium water uptake is higher (100% or more), the values determined here are lower. A sensible explanation for this difference is that the test methods employed are different. In the present work, membranes are exposed to saturated water vapor, whereas prior works rely on weighing membranes after immersion in liquid water, under isothermal conditions. This unexpected difference is fundamentally interesting, since we anticipate that the equilibrium solubility of water in Nexar (at the same degree of sulfonation) should be independent of reservoir state (saturated vapor or liquid) if the states are in equilibrium at the same temperature. One source of error that should be considered in this comparison is that immersion of Nexar in liquid water, followed by surface blotting, does not ensure removal of all excess liquid before weighing, which would naturally result in higher recorded values of Ω_{H_2O}.

In addition to water solubility (a thermodynamic property), water diffusivity (a transport property) can also be discerned by applying Eq. (2) to time-dependent water uptake curves. Values of D in the limit of Fickian diffusion (at relatively short exposure times) are extracted from each pressure increment and are provided for comparison in Fig. 7b for the same systems described in Fig. 7a. Complications reflecting membrane relaxation and/or swelling that accompany mass changes at long exposure times (especially at high RH) are omitted from this analysis. In the case of neat Nexar membranes, D initially increases with increasing water activity and then either reaches a plateau between 10^{-7} and 10^{-8} cm^2/s or displays a shallow maximum over this range. Comparable water diffusion behavior has likewise been reported [36] for a short-chain perfluorosulfonic acid ionomer. In similar fashion as the water solubility results presented in Fig. 7a, the Nexar/IL hybrid membranes exhibit vastly different diffusion behavior. In the Nexar/IL20 membrane, D decreases slightly with increasing water activity and then levels off in almost the same range as neat Nexar (differences are attributed to difficulties in obtaining reliable diffusion results from sorption data collected from membranes that swell substantially), suggesting that the Nexar nanostructure limits the diffusion of water in the hybrid membrane. This conclusion is consistent with the corresponding SAXS profile (*cf.* Fig. 6), which suggests the coexistence of cylindrical and lamellar morphologies. A plausible explanation for this observation is that the population of incorporated [Bmim][BF_4] IL molecules available at this composition is insufficient to fully transform the Nexar nanostructure so that at least some of the neat Nexar morphology remains. Fig. 7b reveals that D measured in the Nexar/IL30 membrane increases monotonically over an order of magnitude as the water activity is increased. Although we do not have SAXS data corresponding to hybrid membranes possessing 30 wt% IL, the Nexar/IL40 membrane appears to possess a single cylindrical morphology according to the results included in Fig. 6. We therefore conclude that differences in Nexar morphology upon addition of the [Bmim][BF_4] IL promote noticeable changes in both water solubility and diffusivity and that these differences are likely to manifest in the molecular transport of penetrant gases, such as CO_2 and N_2 in the next section.

3.5. Gas permeation

To ascertain the extent to which IL-modified Nexar could be used to selectively remove CO_2 from mixed gas streams, single-gas permeation of CO_2 and N_2 has been analyzed at 35 °C through membranes

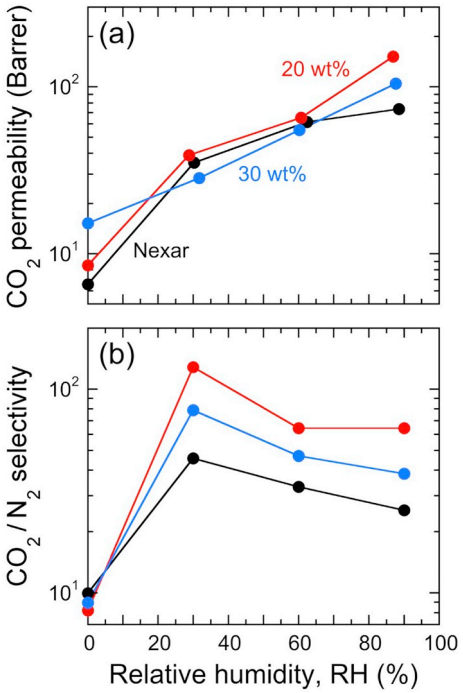

Fig. 8. Single-gas (a) CO_2 permeability and (b) CO_2/N_2 selectivity of neat Nexar and Nexar/IL hybrid membranes presented as functions of RH (labeled according to ω_{IL} and color-coded). The solid lines serve to connect the data. (For interpretation of the references to color in this figure legend, the reader is referred to the Web version of this article.)

containing different amounts of the [Bmim][BF_4] IL under various RH conditions and a feed pressure of 1 bar. In the limit of dry conditions at 0% RH in Fig. 8a, incorporation of the IL into Nexar yields a modest improvement in CO_2 permeability from 6.5 to 15.0 Barrers as ω_{IL} is increased from 0 to 30 wt%. As previously demonstrated, inclusion of water in the feed gas can serve to enhance the permeability of CO_2 through nanostructured polymer membranes containing charged (hydrophilic) diffusive pathways (*e.g.*, Nafion [12] and Nexar [27]). Such improvement, ranging from 6.9 to 17.8x relative to the dry membranes, is evident in Fig. 8a for the three membranes (neat Nexar, Nexar/IL20 and Nexar/IL30) examined. No further benefit of the IL is apparent up to 60% RH. At 90% RH, however, IL-induced differences are manifested, especially with the Nexar/IL20 membrane exhibiting the highest permeability (152 Barrers, which constitutes an increase of ≈1680% relative to the permeability of CO_2 through the same membrane in the dry state). At the same RH, this permeation level is ≈ 100% higher than that of neat Nexar cast from THF (74 Barrers) and ≈53% higher than Nexar cast from a mixed toluene/isopropyl alcohol (TIPA) solvent (99 Barrers), which generates a spherical micelle morphology [19,27]. The reason for the reduction in CO_2 permeability due to an increase in IL content (up to 30 wt%) at 90% RH is not precisely known at this time, but is again believed to be somehow related to the change in Nexar morphology that accompanies incorporation of IL. Single-gas permeability results of N_2 are not included here because they all lie between about 0.5 and 3.0 Barrers. Near the limit of experimental uncertainty, the addition of IL appears to promote a miniscule increase (from about 0.7 to 1.7 Barrers) in N_2 permeability. While the introduction of RH promotes a systematic increase in N_2 permeability in the case of neat Nexar, a minimum is detectable at 30% RH for the two Nexar/IL hybrid membranes. We have previously observed [27] a comparable minimum in N_2 permeability for TIPA-cast Nexar membranes modified with a low-molecular-weight polyethyleneimine and attributed such behavior to incomplete filling of the Nexar morphology. At high RH levels, however, the effect of added IL in Fig. 8a becomes indistinguishable.

The resulting ideal CO_2/N_2 permeability selectivities calculated from the ratio of single-gas CO_2 and N_2 permeabilities are presented in Fig. 8b and, as expected, display maxima at 30% RH (due to the increase in CO_2 permeability and coincident decrease in N_2 permeability) and plateaus at higher RH. These results reveal two important outcomes of this single-gas permeation analysis: (*i*) the maximum ideal selectivity measured here is about 128 (more than or about an order of magnitude improvement over values reported in the literature, *cf.* Table 1) and (*ii*) incorporation of the [Bmim][BF_4] IL consistently improves the ideal CO_2/N_2 selectivity relative to pristine Nexar. Since CO_2 is a known plasticizing agent, however, mixed-gas permeation tests have also been performed on Nexar/IL hybrid membranes at various RH levels with a mixed CO_2/N_2 feed. Results for CO_2 permeability are presented in Fig. 9a and confirm that the addition of IL systematically improves the performance of Nexar in the dry state. In this limit (0% RH), results from the single- and mixed-gas permeation tests are quantitatively comparable: 8.7 *vs.* 8.6 Barrers for the Nexar/IL20 membrane and 15.0 *vs.* 12.0 Barrers for the Nexar/IL30 membrane. Moreover, the presence of water vapor enhances the transport of CO_2 in all the membranes examined, with the highest permeability recorded as 194 Barrers for the case of the Nexar/IL20 membrane evaluated at 100% RH. The data provided in Fig. 9a indicate that the water-induced enhancement of CO_2 permeability in Nexar/IL hybrid membranes (expressed as the ratio of permeabilities measured at the highest and lowest RH levels) is about 22 and 10 for Nexar/IL 20 and Nexar/IL30, respectively, for which the highest RH level is 100%. Comparable results are gleaned from Fig. 8a for single-gas tests conducted up to 90% RH: 18 and 7, respectively.

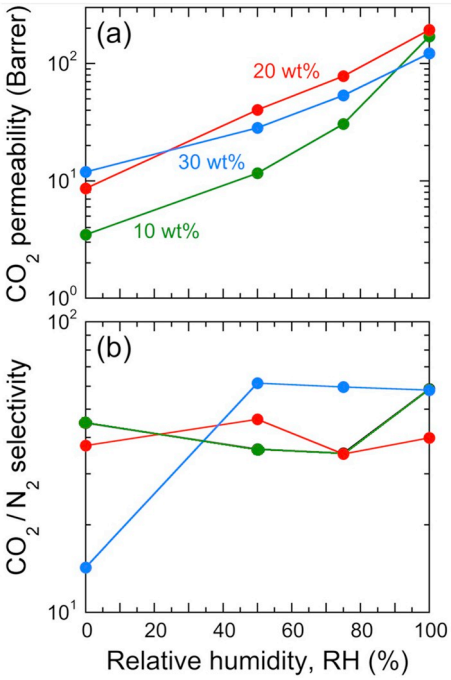

Fig. 9. Mixed-gas (a) CO_2 permeability and (b) CO_2/N_2 selectivity of Nexar/IL hybrid membranes presented as functions of RH (labeled according to ω_{IL} and color-coded). The solid lines serve to connect the data. (For interpretation of the references to color in this figure legend, the reader is referred to the Web version of this article.)

Corresponding CO_2/N_2 separation factors are presented in Fig. 9b and, while most of the measurements lie within the range of 40–60, no definitive trends are apparent. These values qualitatively agree with the ideal selectivities from single-gas permeabilities in the limit of high humidity (although the precise effect of IL addition is inconclusive), but do not exhibit the maxima evident at about 30% RH in Fig. 8b. To facilitate comparison of CO_2 permeabilities and CO_2/N_2 selectivities (separation factors) determined for the Nexar/IL20 and Nexar/IL30 membranes by single- and mixed-gas tests, we combine all the data in Fig. 10a and b, respectively. Two reasons are offered here to explain apparent differences especially at low RH levels: (*i*) the mixed gas stream affords the opportunity for competitive sorption between CO_2 and N_2, and (*ii*) the partial pressure of CO_2 is lower in the mixed gas feed since N_2 serves to dilute the CO_2. It is interesting that the ideal selectivities and separation factors measured here at high RH levels lie in the same range as reported [27] earlier for TIPA-cast Nexar, suggesting that the selectivity of CO_2 relative to N_2 in Nexar membranes is largely governed by the presence of imbibed water, and not the morphological characteristics of the polymer matrix or the addition of hydrophilic compounds such as the [Bmim][BF_4] IL, at high RH.

Two other design factors are considered here: long-term stability, which is critically important for practical consideration, and comparative performance, which provides beneficial insight into future membrane development. In the first instance, a continuous mixed-gas permeation test has been conducted over the course of 72 h with the CO_2/N_2 mixture to elucidate the time-dependent separation

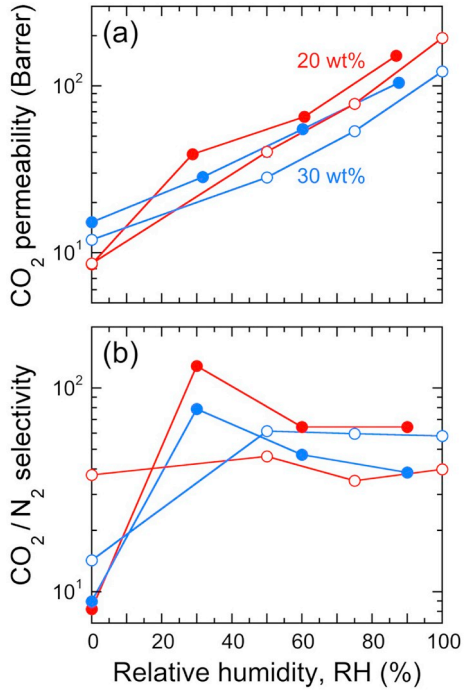

Fig. 10. (a) CO_2 permeability and (b) CO_2/N_2 selectivity of Nexar/IL hybrid membranes measured by single- and mixed-gas permeation tests (filled and open circles, respectively) and presented as functions of RH (labeled according to ω_{IL} and color-coded). The solid lines serve to connect the data. (For interpretation of the references to color in this figure legend, the reader is referred to the Web version of this article.)

performance of the most promising Nexar/IL hybrid membrane containing 20 wt% [Bmim][BF_4] IL at 100% RH. According to the results provided in Fig. 11, the CO_2 permeability undergoes an unexpected change within the first 500 min and then slowly decays with increasing time, whereas the CO_2/N_2 selectivity remains surprisingly constant, over the course of the test. To further interrogate the permanence of the permeability reduction, we have dried and re-tested the same membrane (after 72 h) at 100% RH and find that the CO_2 permeability fully recovers (190 Barrers). This observation strongly suggests that the decay in CO_2 permeability reflects a continuous morphological change or relaxation phenomenon in the hybrid membrane and not IL leakage.

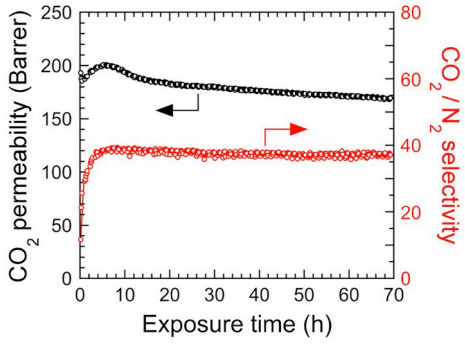

Fig. 11. Long-term performance stability provided as (a) CO_2 permeability and (b) CO_2/N_2 selectivity of the Nexar/IL20 hybrid membrane evaluated at 100% RH.

The second consideration evaluates the gas-separation performance of the Nexar/IL hybrid membranes with respect to state-of-the-art membrane materials. For this purpose, the so-called Robeson plot [37,38], displayed in Fig. 12 for CO_2/N_2 selectivity as a function of CO_2 permeability, is useful. The most important characteristic of this representation is the upper bound identifying the limiting relationship between gas selectivity and gas permeability, which tend to be inversely related. Since a wide range of polymeric membranes have been proposed to separate CO_2 from other gases such as N_2 [8,39–44], only ionomer-based membranes are included in this comparison, which is likewise listed for completeness in Table 1. The presence of water vapor is known to dramatically improve the gas transport properties of several ionomers, including Nexar, Nafion and Aquivion. In the present study, similar results have been obtained from both single- and mixed-gas permeation tests. In the case of Nexar/IL hybrid membranes, however, introduction of water vapor significantly improves CO_2 gas permeability without sacrificing CO_2/N_2 selectivity, resulting in membrane performance that closely approaches the upper bound. We recognize that a higher CO_2 permeability ($\approx$390 Barrers) is achieved with Nafion at $\sim$100% RH [12], but the corresponding CO_2/N_2 selectivity is only $\approx$30, which is significantly less than the value we report here for Nexar/IL hybrid membranes.

4. Conclusions

In the present work, hybrid membranes composed of a block ionomer and an IL have been fabricated by physically blending a mid-block-sulfonated pentablock polymer with the [Bmim][BF_4] IL. The thermal, chemical, morphological, sorption, and permeability attributes of the resultant membranes have been examined through the use of a battery of different analytical methods to evaluate the potential of these materials as gas-separation membranes. Thermogravimetric analysis demonstrates that incorporation of IL into Nexar noticeably improves the thermal stability of these hybrid membranes at temperatures both below and above the decomposition temperature, whereas spectra acquired by FTIR spectroscopy reveal that the sulfonic acid groups of Nexar do not chemically interact with the IL. Complementary morphological characterization by SAXS indicates that addition of IL to Nexar promotes nanostructural (*i*) swelling as discerned from *d*-spacing measurements and (*ii*) ordering due to an increase in the number of scattering peaks. Moreover, the added IL induces a transition from coexisting cylindrical + lamellar morphologies at relatively low IL loading levels (10 and 20 wt% IL) to a single cylindrical morphology at the highest loading level investigated (40 wt% IL). Water sorption studies provide evidence that a single Nexar morphology (presumably in membranes with 30 wt% IL) is required to achieve both high water solubility and diffusivity levels. Addition of the [Bmim][BF_4] IL into Nexar systematically increases CO_2 permeability through the hybrid membrane in the dry state at 0% RH. Introduction of water vapor into the gas feed further promotes CO_2 transport in the membrane, as independently ascertained by single- and mixed-gas permeation tests. A maximum CO_2 permeability of $\approx$190 Barrers determined at 90% RH represents a significantly improved level of performance (> 20x higher) relative to the same membrane in dry state. Compared with other ionomers, Nexar-based membranes exhibit higher and stable CO_2/N_2 selectivities ($\sim$50), combined with acceptably high CO_2 permeabilities, and are therefore suitable for CO_2/N_2 separation. In summary, the results reported here provide a fundamental understanding of the morphological characteristics and property development in Nexar/IL hybrid membranes prepared at various loading levels and subjected to different RH levels

Table 1
CO_2/N_2 separation performance of selected ionomer-based membranes.

Membrane	P_{CO_2}*(Barrer)*	α_{CO_2/N_2}	*Ref.*
Nexar-H	15	15	[26] [a]
Nexar-K	27	11	[26]
Nexar-Na	25	12	[26]
Nexar-Ca	22	12	[26]
Nexar-Li	12	15	[26]
Nexar	28	–	[15] [b]
Aquivion (75% RH)	120	36	[45] [c]
Nafion 117 (dry)	2.3	9.6	[46] [d]
Nafion 117 (dry)	2.4	9.2	[47] [e]
Nexar	18	33	[27] [f]
Nexar	99	58	[27] [g]
Nafion (cast, dry)	1.6	8.9	[12] [h]
Nafion/[Bmim][BF_4], 40 wt% (dry)	75	35	[12] [h]
Nafion (cast, 100% RH)	209	15	[12] [i]
Nafion/[Bmim][BF_4], 40 wt% (100% RH)	390	30	[12] [i]
Nexar/[Bmim][BF_4], 20 wt% (30% RH, single gas)	36	128	This work
Nexar/[Bmim][BF_4], 20 wt% (100% RH, single gas)	153	64	This work [j]
Nexar/[Bmim][BF_4], 20 wt% (100% RH, mixed gas)	194	40	This work [k]
Nexar/[Bmim][BF_4], 30 wt% (30% RH, single gas)	28	79	This work
Nexar/[Bmim][BF_4], 30 wt% (100% RH, mixed gas)	122	58	This work

[a] Single-gas permeation test conducted with a feed pressure of 4 atm at 40 °C. Gas permeability data estimated from the TOC of ref. [26].
[b] Single-gas permeation test conducted with a feed pressure of 4 atm at 30 °C.
[c] Single-gas permeation test conducted with a feed pressure of 2 bar at 25 °C, gas permeability data estimated from Figs. 4 and 7 from Ref. [45].
[d] Single-gas permeation test conducted with a feed pressure of 2 atm at 35 °C.
[e] Single-gas permeation test conducted with a feed pressure of 1 atm 35 °C.
[f] Single-gas permeation test conducted with a feed pressure of 1 atm 35 °C, dry state.
[g] Single-gas permeation test conducted with a feed pressure of 1 atm 35 °C, wet state.
[h] Single-gas permeation test conducted with a feed pressure of 2 bar at ambient temperature.
[i] CO_2/N_2 mixed-gas (10/90 v/v) permeation test conducted with a feed pressure of 2 bar at ambient temperature.
[j] Single-gas permeation test conducted with a feed pressure of 1 atm, 35 °C.
[k] CO_2/N_2 mixed-gas (10/90 v/v) permeation test performed with a feed pressure of 2 bar at ambient temperature.

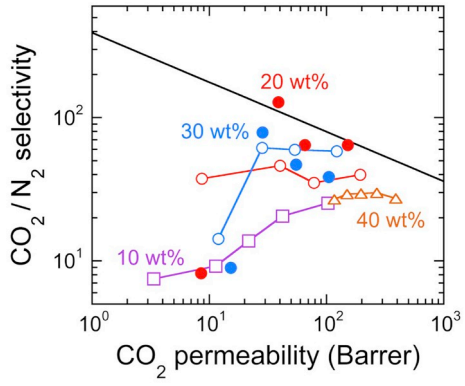

Fig. 12. CO_2 separation performance of Nexar/IL hybrid membranes measured by single- and mixed-gas permeation tests (filled and open circles, respectively) and compared with Nafion/IL hybrid membranes tested by mixed-gas permeation at different ω_{IL} (squares and triangles; color-coded). The diagonal line represents the Robeson upper bound [37,38], and the color-coded solid lines serve to connect the data. (For interpretation of the references to color in this figure legend, the reader is referred to the Web version of this article.)

to expedite the future design of gas-separation membranes derived from nanostructured ionomers.

Conflicts of interest

The authors declare no conflicts.

Acknowledgments

This work was supported by the Horizon 2020 Research and Innovation program of the European Union (Grant No. 727734) and the CLIMIT program of the Research Council of Norway (Grant No. 254791). We also thank the NC State Nonwovens Institute for financial support and Dr. B. Lee at Argonne National Laboratory for technical assistance. This research used resources of the Advanced Photon Source, a U.S. Department of Energy (DOE) Office of Science User Facility operated for the DOE Office of Science by Argonne National Laboratory under Contract No. DE-AC02-06CH11357.

References

[1] A. Brunetti, F. Scura, G. Barbieri, E. Drioli, Membrane technologies for CO_2 separation, J. Membr. Sci. 359 (2010) 115–125.
[2] N. MacDowell, N. Florin, A. Buchard, J. Hallett, A. Galindo, G. Jackson, C.S. Adjiman, C.K. Williams, N. Shah, P. Fennell, An overview of CO_2 capture technologies, Energy Environ. Sci. 3 (2010) 1645–1669.
[3] M.H. Ibrahim, M.H. El-Naas, Z. Zhang, B. Van der Bruggen, CO_2 capture using hollow fiber membranes: a review of membrane wetting, Energy Fuels 32 (2018) 963–978.
[4] Z. Dai, J. Deng, L. Ansaloni, S. Janakiram, L. Deng, Thin-film-composite hollow fiber membranes containing amino acid salts as mobile carriers for CO_2 separation, J. Membr. Sci. 578 (2019) 61–68.
[5] S. Rafiq, L. Deng, M.-B. Hägg, Role of facilitated transport membranes and composite membranes for efficient CO_2 capture – a review, ChemBioEng Reviews 3 (2016) 68–85.
[6] W.J. Koros, C. Zhang, Materials for next-generation molecularly selective synthetic membranes, Nat. Mater. 16 (2017) 289.
[7] Z. Qiao, S. Zhao, M. Sheng, J. Wang, S. Wang, Z. Wang, C. Zhong, M.D. Guiver, Metal-induced ordered microporous polymers for fabricating large-area gas separation membranes, Nat. Mater. 18 (2019) 163–168.
[8] Z. Dai, R.D. Noble, D.L. Gin, X. Zhang, L. Deng, Combination of ionic liquids with membrane technology: a new approach for CO_2 separation, J. Membr. Sci. 497 (2016) 1–20.
[9] L.C. Tomé, I.M. Marrucho, Ionic liquid-based materials: a platform to design engineered CO_2 separation membranes, Chem. Soc. Rev. 45 (2016) 2785–2824.

[10] T.P. Lodge, A unique platform for materials design, Science 321 (2008) 50–51.
[11] M.G. Cowan, D.L. Gin, R.D. Noble, Poly(ionic liquid)/ionic liquid ion-gels with high "free" ionic liquid content: platform membrane materials for CO_2/light gas separations, Acc. Chem. Res. 49 (2016) 724–732.
[12] Z. Dai, L. Ansaloni, J.J. Ryan, R.J. Spontak, L. Deng, Nafion/IL hybrid membranes with tuned nanostructure for enhanced CO_2 separation: effects of ionic liquid and water vapor, Green Chem. 20 (2018) 1391–1404.
[13] Y.A. Elabd, M.A. Hickner, Block copolymers for fuel cells, Macromolecules 44 (2010) 1–11.
[14] M.J. Park, N.P. Balsara, Phase behavior of symmetric sulfonated block copolymers, Macromolecules 41 (2008) 3678–3687.
[15] Y.F. Fan, C.J. Cornelius, Raman spectroscopic and gas transport study of a pentablock ionomer complexed with metal ions and its relationship to physical properties, J. Mater. Sci. 48 (2013) 1153–1161.
[16] P. Knychała, K. Timachova, M. Banaszak, N.P. Balsara, 50th anniversary perspective: phase behavior of polymer solutions and blends, Macromolecules 50 (2017) 3051–3065.
[17] I.W. Hamley (Ed.), Developments in Block Copolymer Science and Technology, Wiley, New York, 2004.
[18] P.J. Griffin, G.B. Salmon, J. Ford, K.I. Winey, Predicting the solution morphology of a sulfonated pentablock copolymer in binary solvent mixtures, J. Polym. Sci. B: Polym. Phys. 54 (2016) 254–262.
[19] K.P. Mineart, X. Jiang, H. Jinnai, A. Takahara, R.J. Spontak, Morphological investigation of midblock-sulfonated block ionomers prepared from solvents differing in polarity, Macromol. Rapid Commun. 36 (2015) 432–438.
[20] K.P. Mineart, J.J. Ryan, M.-S. Appavou, B. Lee, M. Gradzielski, R.J. Spontak, Self-sssembly of a midblock-sulfonated pentablock copolymer in mixed organic solvents: a combined SAXS and SANS analysis, Langmuir 35 (2019) 1032–1039.
[21] K.P. Mineart, B. Lee, R.J. Spontak, A solvent-vapor approach toward the control of block ionomer morphologies, Macromolecules 49 (2016) 3126–3137.
[22] G.M. Geise, B.D. Freeman, D.R. Paul, Characterization of a sulfonated pentablock copolymer for desalination applications, Polymer 51 (2010) 5815–5822.
[23] J. Yeo, S.Y. Kim, S. Kim, D.Y. Ryu, T.H. Kim, M.J. Park, Mechanically and structurally robust sulfonated block copolymer membranes for water purification applications, Nanotechnology 23 (2012) 245703.
[24] G.M. Shi, J. Zuo, S.H. Tang, S. Wei, T.S. Chung, Layer-by-layer (LbL) polyelectrolyte membrane with Nexar™ polymer as a polyanion for pervaporation dehydration of ethanol, Separ. Purif. Technol. 140 (2015) 13–22.
[25] J. Zuo, G.M. Shi, S. Wei, T.-S. Chung, The development of novel Nexar block copolymer/Ultem composite membranes for C2–C4 alcohols dehydration via pervaporation, ACS Appl. Mater. Interfaces 6 (2014) 13874–13883.
[26] Y. Fan, M. Zhang, R.B. Moore, C.J. Cornelius, Structure, physical properties, and molecule transport of gas, liquid, and ions within a pentablock copolymer, J. Membr. Sci. 464 (2014) 179–187.
[27] L. Ansaloni, Z. Dai, J.J. Ryan, K.P. Mineart, Q. Yu, K.T. Saud, M.-B. Hägg, R.J. Spontak, L. Deng, Solvent-templated block ionomers for base- and acid-gas separations: effect of humidity on ammonia and carbon dioxide permeation, Adv. Mater. Interf. 4 (2017) 1700854.
[28] L.C. Antoine, Vapor Pressure: a new relationship between pressure and temperature, Proc. Acad. Sci. 107 (1888) 681–685.
[29] D.G. Pye, H.H. Hoehn, M. Panar, Measurement of gas permeability of polymers. I. permeabilities in constant volume/variable pressure apparatus, J. Appl. Polym. Sci. 20 (1976) 1921–1931.
[30] Z. Dai, H. Aboukeila, L. Ansaloni, J. Deng, M. Giacinti Baschetti, L. Deng, Nafion/PEG hybrid membrane for CO_2 separation: effect of PEG on membrane microstructure and performance, Separ. Purif. Technol. 214 (2019) 67–77.
[31] Q. Deng, C.A. Wilkie, R.B. Moore, K.A. Mauritz, TGA–FTi.r. investigation of the thermal degradation of Nafion® and Nafion®/[silicon oxide]-based nanocomposites, Polymer 39 (1998) 5961–5972.
[32] C.P. Fredlake, J.M. Crosthwaite, D.G. Hert, S.N.V.K. Aki, J.F. Brennecke, Thermophysical properties of imidazolium-based ionic liquids, J. Chem. Eng. Data 49 (2004) 954–964.
[33] S.A. Dharaskar, K.L. Wasewar, M.N. Varma, D.Z. Shende, C. Yoo, Synthesis, characterization and application of 1-butyl-3-methylimidazolium tetrafluoroborate for extractive desulfurization of liquid fuel, Arabian J. Chem. 9 (2016) 578–587.
[34] J.J. Ryan, K.P. Mineart, B. Lee, R.J. Spontak, Ordering and grain growth in charged block copolymer bulk films: a comparison of solvent-related processes, Adv. Mater. Interf. 5 (2018) 1701667.
[35] K.P. Mineart, J.D. Dickerson, D.M. Love, B. Lee, X. Zuo, R.J. Spontak, Hydrothermal conditioning of physical hydrogels prepared from a midblock-sulfonated multiblock copolymer, Macromol. Rapid Commun. 38 (2017) 1600666.
[36] M. De Angelis, S. Lodge, M.G. Baschetti, G. Sarti, F. Doghieri, A. Sanguineti, P. Fossati, Water sorption and diffusion in a short-side-chain perfluorosulfonic acid ionomer membrane for PEMFCS: effect of temperature and pre-treatment, Desalination 193 (2006) 398–404.
[37] L.M. Robeson, Correlation of separation factor versus permeability for polymeric membranes, J. Membr. Sci. 62 (1991) 165–185.
[38] L.M. Robeson, The upper bound revisited, J. Membr. Sci. 320 (2008) 390–400.
[39] H.B. Park, J. Kamcev, L.M. Robeson, M. Elimelech, B.D. Freeman, Maximizing the right stuff: the trade-off between membrane permeability and selectivity, Science (2017) 356 eaab0530.
[40] Z. Dai, L. Ansaloni, L. Deng, Recent advances in multi-layer composite polymeric membranes for CO_2 separation: a review, Green Energy Environ. 1 (2016) 102–128.
[41] S. Janakiram, M. Ahmadi, Z. Dai, L. Ansaloni, L. Deng, Performance of nanocomposite membranes containing 0D to 2D nanofillers for CO_2 separation: a review, Membranes 8 (2018) 24.
[42] M. Ahmadi, S. Janakiram, Z. Dai, L. Ansaloni, L. Deng, Performance of mixed matrix membranes containing porous two-dimensional (2D) and three-dimensional (3D) fillers for CO_2 separation: a review, Membranes 8 (2018) 50.
[43] H. Lin, B.D. Freeman, Materials selection guidelines for membranes that remove CO_2 from gas mixtures, J. Mol. Struct. 739 (2005) 57–74.
[44] N.P. Patel, A.C. Miller, R.J. Spontak, Highly CO_2-permeable and selective polymer nanocomposite membranes, Adv. Mater. 15 (2003) 729–733.
[45] M. Giacinti Baschetti, M. Minelli, J. Catalano, G.C. Sarti, Gas permeation in perflurosulfonated membranes: influence of temperature and relative humidity, Int. J. Hydrogen Energy 38 (2013) 11973–11982.
[46] K.A. Mauritz, R.B. Moore, State of understanding of nafion, Chem. Rev. 104 (2004) 4535–4586.
[47] J.S. Chiou, D.R. Paul, Gas permeation in a dry Nafion membrane, Ind. Eng. Chem. Res. 27 (1988) 2161–2164.